Frontiers in Heat and Mass Transfer

Tech Science Press

Doi:10.32604/fhmt.2025.059466

ARTICLE

On Heat Transfer in Oblique Stagnation Point Nanofluid Flow with Temperature Dependent Viscosity

Rabail Tabassum[1], M. Kamran[1], Khalil Ur Rehman[2,*], Wasfi Shatanawi[2,3] and Rashid Mehmood[4]

[1]Department of Mathematics, Faculty of Basic and Applied Sciences, Air University, Islamabad, 44000, Pakistan
[2]Department of Mathematics and Sciences, College of Humanities and Sciences, Prince Sultan University, Riyadh, 11586, Saudi Arabia
[3]Department of Mathematics, Faculty of Science, The Hashemite University, Zarqa, 13133, Jordan
[4]Department of Mathematics, Faculty of Applied Sciences, HITEC University, Rawalpindi, 47080, Pakistan

*Corresponding Author: Khalil Ur Rehman. Email: kurrehman@psu.edu.sa

Received: 09 October 2024; Accepted: 15 January 2025; Published: 25 April 2025

ABSTRACT: This study aims to elucidate the connection between the shape factor of GO (graphene oxide) nanoparticles and the behavior of blood-based non-aligned, 2-dimensional, incompressible nanofluid flow near stagnation point, under the influence of temperature-dependent viscosity. Appropriate similarity transformations are employed to transform the non-linear partial differential equations (PDEs) into ordinary differential equations (ODEs). The governing equations are subsequently resolved by utilizing the shooting method. The modified Maxwell model is used to estimate the thermal efficiency of the nanofluid affected by different nanoparticle shapes. The impact of various shapes of GO nanoparticles on the velocity and temperature profiles, along with drag forces and heat flux at the stretching boundary, are examined with particular attention to factors such as viscosity changes. Numerical findings are based on the constant concentration of ϕ = 5% with nanoparticles measuring 25 nm in size. The influence of different shapes of GO nanoparticles is analyzed for velocity, temperature distributions, as well as drag forces, and heat transfer at the stretching boundary. The velocity profile is highest for spherical-shaped nanoparticles, whereas the blade-shaped particles produced the greatest temperature distribution. Additionally, it was observed that enhancing the nanoparticles' volume fraction from 1% to 9% significantly improved the temperature profile. Streamline trends are more inclined to the left when the stretching ratio parameter B = 0.7 is applied, and a similar pattern is noted for the variable viscosity case with m = 0.5. Furthermore, the blade-shaped nanoparticles exhibit the highest thermal conductivity, while the spherical-shaped nanoparticles display the lowest.

KEYWORDS: Heat transfer; nanofluids; oblique flows; variable viscosity; Runge-Kutta-Fehlberg scheme

1 Introduction

Nanofluids are fluids that contain nanoparticles, which are particles at the nanometer scale. These fluids are colloidal suspensions of nanoparticles, typically composed of oxides, metals, and carbides. Nanofluids possess unique properties that make them valuable in various heat transfer applications, such as in microelectronics, fuel cells, pharmaceutical processes, hybrid engines, engine cooling/vehicle thermal management, household refrigerators, radiators, and more. Some key research areas involving nanofluids include studies on the impact of physical parameters on their thermal conductivity. For example, Jang et al. [1] focused on how these parameters affect nanofluid conductivity and were the first to model the Brownian motion-induced nano convection, highlighting its significance as a crucial mechanism at the nanoscale. Li et al. [2] concentrated on the advancement of nanofluids, exploring their synthesis and characterization in

stationary conditions. Aybar et al. [3] examined the thermal conductivity of nanofluids, highlighting the influence of factors like temperature, and explored mechanisms that enhance thermal conductivity, such as Brownian motion. Tabassum et al. [4] investigated the impact of variable viscosity on the flow characteristics of inclined nanofluid flows containing copper nanoparticles. It was found that the viscosity parameter leads to a decrease in the surface friction coefficient. Arshad et al. [5] conducted a comprehensive study of graphene-based nanofluids: synthesis, analysis, and various applications. They also studied the changes in the behavior of nano-sized graphene particles in different carrier fluids. Hatami et al. [6] discussed the theories of various suspension nanoparticles. Various researchers observed an increase in thermal conductivity after adding nanoparticles. Hatami et al. [7] analyzed the practical applications of nanofluids through experimental and numerical analysis. They focused on cooling and heating applications, i.e., micro-ducts and heating and air conditioning models. Li et al. [8] conducted a comprehensive study from three aspects, i.e., influencing factors, prediction models, and practical applications.

In fluid mechanics, a stagnation point refers to a point on a surface where the velocity is zero. The flow around this point is known as stagnation flow. Oblique stagnation flow occurs when the fluid approaches the surface at an acute angle. Flow over an expanding surface refers to the flow exiting a slot, which can be modeled as a boundary layer emerging from the slot. Viscosity, which depends on temperature, has different relationships for different substances: for liquids, viscosity decreases as temperature increases, while for solids, it increases with temperature. The skin friction coefficient represents the resistance an object experiences from a surface it contacts, defined as the ratio of the frictional force to the normal force. Heat flux is the rate at which heat is transferred from a hotter area to a cooler one through a material over a given time. Researchers have studied stagnation points in various contexts, such as Reza et al. [9], who investigated the oblique stagnation point flow of a two-dimensional stationary incompressible viscous fluid towards a slender boundary, noting that the distance from the stagnation point is directly influenced by velocity, and shear force is inversely proportional to the zero velocity point. Mahapatra et al. [10] also studied the two-dimensional stationary oblique stagnation point flow of an incompressible viscous fluid towards a slender surface. The extended studies on stagnation point flow can be assessed in Refs. [11–13]. Ghaffar [14] discussed the stagnation flow in the oblique geometry of a Newtonian suspension on various boundaries, including stretching sheet, vertical surface, and shrinking sheet. Special effects of germane parameters are noticed and the results of the transformed equations are compared with exact solutions. Lok et al. [15] investigated the magneto-hydrodynamic flow impinging on an extensible surface, the impression of MHD upon flow is noted by a displacement in the stagnation line. Specifically, when dealing with a shrinking surface, there's an observation of a reversed flow region close to the wall. This suggests that MHD influences not only the stagnation line but also induces a distinct reversed flow zone near the wall when the surface is shrinking. Ghaffari et al. [16] researched the effects of non-linear radiation on the slanting stagnation flow of Maxwell fluid. The study elucidates a notable correlation between temperature and thermal transport rate. Moreover, it demonstrates the direct relationship between a physical parameter, i.e., Prandtl number and heat transfer rate Bano et al. [17] discussed the slanted stagnation flow of a dense fluid with thermal transfer towards an extended cylinder. It explains how the fluid influences obliquely upon the surface of the cylinder. The graphical representation of temperature and velocity profiles are illustrated and further examined for the effects of related parameters.

A very important property of fluids that plays a vital role in the flow regime is viscosity. Viscosity depends strongly on temperature. In liquids, it depicts an inverse relationship with temperature whereas a direct relationship with temperature is observed in gases. Temperature dependence on viscosity is important for various applications e.g., Increase in temperatures causes an increase in the attractive forces between particles which helps them to overcome the surrounding forces. A daily life example is cooking oil moving

more fluidly in hot utensils than in a cold one. Here are a few explorations in which viscosity variation is studied. Booker [18] explored thermal convection in fluids with viscosity that is highly dependent on temperature. They examined the effects on both free and rigid boundaries, observing that the flow is three-dimensional at a free upper boundary, while it is nearly two-dimensional with a rigid upper boundary. Wall et al. [19] investigated the linear stability of channel flow in fluids with temperature-dependent viscosity, focusing on three material effects: bulk effects, velocity-profile shape effects, and thin-layer effects. Nguyen et al. [20] examined viscosity variations in water-based nanofluids based on temperature and particle size, applying the phenomena of Couette flow to a viscometer for their results. Prasad et al. [21] studied the impact of variable viscosity on magnetohydrodynamic (MHD) viscoelastic fluid flow and heat transfer over a stretching sheet, finding that an increase in the magnetic field parameter leads to a decrease in the temperature profile. They also identified an inverse relationship between skin friction and magnetic field parameters. Anjali Devi et al. [22] investigated the effects of temperature-dependent viscosity and thermal conductivity on hydromagnetic flow, focusing on physical parameters such as skin friction coefficient, temperature, velocity, and heat transfer rates. Huda et al. [23] analyzed temperature-dependent viscosity in nanofluids with shape factors over a heated tube, finding that the velocity of the nanofluid increased. Alabdan et al. [24] examined the flow of a couple stress nanofluid over an oscillatory stretching surface, noting temperature changes in viscosity and thermal Biot numbers, and observing that the skin friction coefficient periodically increased with the viscosity vector and couple stress parameter. Ahmad et al. [25] stressed the relationships between viscosity as a function of temperature, thermal conductivity, and exothermic catalytic processes. In the context of these chemical interactions, the parameters have a significant impact on temperature distribution, mass concentration patterns, and velocity profiles.

The shape factor of nanoparticles is a measure of their geometry or form, which affects their interaction with the surrounding fluid. For instance, nanoparticles can have different shapes spherical, rod-like (elongated), plate-like, or other complex forms. Each shape influences how the nanofluid behaves, such as how it conducts heat, flows, or interacts with surfaces. Shape factors often refer to geometric parameters or characteristics of nanoparticles dispersed within the fluid. These factors can influence the heat transfer, rheological properties, and behavior of the nanofluid. Shape factors play a vital role in modeling the thermal conductivity, viscosity, and other properties of nanofluids. Researchers frequently consider these factors when studying and designing nanofluids for various applications, ranging from electronic cooling to biomedical treatments, as different shapes can lead to varying performance characteristics. Several studies have explored viscosity variation in nanofluids. Sheikholeslami et al. [26] examined the effect of shape factors on nanofluids in a porous medium, finding that the Hartmann number is inversely related to the nanofluid velocity and Nusselt number. Waqas et al. [27] highlighted the significance of shape factors in Sisko nanofluids, with their results showing that the velocity profile decreases as the velocity slip parameter increases. Additionally, the temperature profile of the nanofluids increases with both the thermal radiation parameter and the nanoparticle volume fraction. Hayat et al. [28] investigated the impact of particle shape on flow and heat transfer, offering an extensive discussion on the influence of various factors such as unsteadiness, magnetic parameter, and Eckert number. Both velocity and temperature are affected by the shape of nanoparticles, which leads to optimal flow and heat transfer.

Velocity slip highlights the discrepancy in velocity between a fluid and its solid boundary. Discrepancy means that the fluid that adjacent to the solid surface does not stick to it but rather shows relative motion with it. Velocity slip is strongly impacted by fluid traits, boundary features, and flow dynamics. Practically, its vital comprehension extends to microfluidics and rarefied gas analysis, challenging conventional presumptions. Integrating slip velocity into predictive frameworks enables more nuanced understandings of fluid behavior, driving innovation in practical domains. Here are some areas of exploration in which velocity slip condition

is studied. Khan et al. [29] emphasized the study of phase flow characteristics in MHD nanofluids, incorporating the effects of slip on oscillatory slanted stagnation flow under an inclined magnetic field. His study compared the behaviors of nanoparticles made of Copper, Alumina, and Titania, using water as the carrier fluid, and found that copper nanoparticles enhanced the magnetic susceptibility of the nanofluid. Rizwana et al. [30] explored the slip effects on time-independent tilted stagnation point flow of nanofluids under an oblique magnetic field, observing that the Casson fluid parameter accelerates fluid motion. Additionally, Joule heating and dissipation were found to raise the system's temperature. Kolsi et al. [31] focused on the thermal development of ethylene glycol-based material by adding a hybrid nanofluid for slip flow at an oblique stagnation point, noting a strong influence of slip intensity on temperature and velocity profiles. Mandal et al. [32] conducted a numerical simulation on mixed convective and arbitrary oblique stagnation point slip flow of an MHD fluid, revealing that the magnetic field amplifies skin friction as flow obliqueness increases. Bai et al. [33] studied the variable MHD oblique stagnation slip flow of nanofluids, incorporating the Cattaneo-Christov double diffusion and Buongiorno models, and observed that nanoparticle diffusion, through thermophoresis and Brownian motion, affects concentration and energy and mass transfer, with advection and radiation aiding thermal transmission. Rahman et al. [34] examined the oblique stagnation-point flow of a nanofluid past a shrinking sheet, noting that shrinking parameters and dimensionless strain rates shift the point of zero skin friction on a stretching sheet, with increasing strain rate leading to oblique flow towards the surface. Their study also suggested the existence of dual solutions for the opposing flow case. Abbas et al. [35] studied the stagnation flow of a micropolar nanofluid past a circular cylinder with velocity and thermal slip, finding that copper-water nanofluids exhibited the highest skin friction and heat transfer rates compared to titanium-water and alumina-water nanofluids.

Benkhedda et al. [36] presented a numerical investigation of time-independent forced convective heat transfer and fluid flow of a hybrid nanofluid through an isothermally heated flat tube, considering various nanoparticle shapes. Using the finite volume method in cylindrical coordinates and solving with a FORTRAN program, their study found that platelet-shaped nanoparticles yielded the highest friction factor values, especially at volume fractions ranging from 0% to 8%. Kata et al. [37] examined the enhanced thermal characteristics of a hybrid nanofluid composed of Al_2O_3 (alumina) and Ag (silver) nanoparticles suspended in a 50%–50% mixture of $C_2H_6O_2$-H_2O, impacting obliquely on an elastic surface under a magnetic field. They found that the thermal energy transfer rate in the hybrid nanofluid increased by 11.5% compared to spherical particles when using blade-shaped nanoparticles. Li et al. [38] investigated the effect of the shape factor on a mass-based hybrid nanofluid model for Homann stagnation-point flow in porous media, using the HAM-based Mathematica package BVPh 2.0 to approximate solutions for coupled nonlinear ordinary differential equations. Their results showed that platelet-shaped nanoparticles in the hybrid nanofluid model produced the highest heat transfer rates and minimal surface friction, with skin friction coefficient values ranging from 2.03443 to 3.10222 depending on the permeability coefficient. Rafique et al. [39] studied the influence of nanoparticle shapes on the entropy production of a water-alumina nanofluid flowing over a permeable, MHD stretching sheet with quadratic velocity profiles, factoring in viscous dissipation and Joule heating effects. Their results indicated a 6.3% increase in wall shear stress as nanoparticle volume fraction increased from 0% to 2%, with further increases as the fraction rose from 2% to 4%. Additionally, when the magnetic effect accounted for about 5% of the boundary layer flow, the convective heat transfer rate increased by approximately 16.4%. Rosalind Mary et al. [40] explored the thermal applications of magnetized hybrid nanomaterials by evaluating the effects of different nanoparticle shapes. Their study, using a 50:50 mixture of ethylene glycol ($C_2H_6O_2$) and water (H_2O) with silver and alumina nanoparticles, showed that both mono and hybrid nanofluid temperature profiles increased with nanoparticle volume fraction and Biot number.

Carbon-based nanomaterial GO has unique properties such as high surface area, excellent conductivity, and the ability to interact with biological systems. In thermal therapy and drug delivery, graphene oxide-based nanofluids are injected into the bloodstream to deliver drugs or thermal energy to tumors. The shape of **graphene oxide nanoparticles** in nanofluids significantly influences the flow characteristics and fluid dynamics properties. By modifying the shape of the graphene oxide, we can optimize nanofluid thermal efficiency. The viscosity of a fluid, particularly one containing suspended nanoparticles such as graphene oxide, varies with temperature. Understanding how viscosity changes with temperature is essential for analyzing heat transfer in dynamic systems. This temperature dependence affects the fluid's flow behavior and heat thermal efficiency. The existing research on oblique nanofluid flows conveys that less consideration has been paid to towards investigation of the heat transport phenomenon influenced by viscosity variation and various shape features of GO nanoparticles. In the current exploration we are aiming to study the influence of variation in GO nanoparticle shapes and viscosity upon the heat transport characteristics and velocity profile of blood based oblique nanofluid flow in neighborhood of stagnation-point that has not been investigated before.

Although significant research has been conducted on the analysis of nanoparticles shape factors, limited studies have investigated the heat transfer behavior in oblique stagnation point flow influenced by these shape factors. This study seeks to examine this concept more thoroughly by addressing the following questions:

- What effects do different nanoparticle shapes have on both primary and secondary flow profiles, as well as temperature distribution?
- How do variations in porosity and viscosity affect the flow characteristics?

2 Problem Formulation

We are taking a stationary state, 2D non-compressible, non-aligned transport of blood-based nanofluid containing graphene oxide nano-sized particles with viscosity depending upon the temperature in the vicinity of the stagnation point. Nanofluid strikes the stretching surface obliquely and occupies the region above the horizontal axis. Here blood is used as a carrier liquid and its viscosity changes substantially with temperature variation, therefore modified form of (the Brinkman) viscosity model is incorporated to examine the viscosity varying with respect to temperature. The nanoparticles different shapes play a crucial role in determining the heat transfer properties of nanofluids for that reason different shapes of GO nanoparticles of size 25 nm are added to improve the heat transfer performance. Two opposing forces of equal magnitude are plotted on $\check{x}$-axis so that the origin remains fixed on the extending surface in Fig. 1. For the considered problem, the steady conservation of mass, energy equations, and momentum can be written as follows (neglecting viscous dissipation):

$$\frac{\partial \check{u}^*}{\partial \check{x}^*} + \frac{\partial \check{v}^*}{\partial \check{y}^*} = 0, \tag{1}$$

$$\check{u}^* \frac{\partial \check{u}^*}{\partial \check{x}^*} + \check{v}^* \frac{\partial \check{u}^*}{\partial \check{y}^*} + \frac{1}{\check{\rho}_{nf}} \frac{\partial \check{p}^*}{\partial \check{x}^*} = \frac{\mu_{nf}\left(\check{T}^*\right)}{\check{\rho}_{nf}} \frac{\partial^2 \check{u}^*}{\partial \check{y}^{*2}} + \frac{1}{\check{\rho}_{nf}} \frac{\partial \check{u}^*}{\partial \check{y}^*} \frac{\partial \mu_{nf}\left(\check{T}^*\right)}{\partial \hat{T}^*} \frac{\partial \check{T}^*}{\partial \check{y}^*}, \tag{2}$$

$$\check{u}^* \frac{\partial \check{v}^*}{\partial \check{x}^*} + \hat{v}^* \frac{\partial \check{v}^*}{\partial \check{y}^*} + \frac{1}{\check{\rho}_{nf}} \frac{\partial \check{\rho}^*}{\partial \check{y}^*} = \frac{\mu_{nf}\left(\check{T}^*\right)}{\check{\rho}_{nf}} \frac{\partial^2 \check{v}^*}{\partial \check{y}^{*2}} + \frac{1}{\check{\rho}_{nf}} \frac{\partial \check{v}^*}{\partial \check{y}^*} \frac{\partial \mu_{nf}\left(\check{T}^*\right)}{\partial \check{T}^*} \frac{\partial \check{T}^*}{\partial \check{y}^*}, \tag{3}$$

$$\left(\check{\rho} c_{\check{\rho}}\right)_{nf} \left(\check{u}^* \frac{\partial \check{T}^*}{\partial \check{x}^*} + \check{v}^* \frac{\partial \check{T}^*}{\partial \check{y}^*}\right) = \check{k}_{nf} \frac{\partial^2 \check{T}^*}{\partial \check{y}^{*2}}, \tag{4}$$

where $\mu_{nf}\left(\check{T}^*\right) = \frac{\mu_0 e^{-d\left(\check{T}^* - \check{T}_\infty\right)}}{(1-\phi)^{2.5}}$ is the viscosity of nanofluid as a function of temperature, d denotes the viscosity variation exponent, $\check{T}^*, \mu_0, \check{T}_\infty$ and ϕ are representing the temperature, reference viscosity ambient temperature of nanofluid and nano-particles volume fraction. Additionally, nanofluid's density, pressure, thermal conductivity and specific heat are denoted by $\check{\rho}_{nf}$, $\check{p}^*$, $\check{k}_{nf}$. The velocity components are denoted by $\check{u}^*$ and $\check{v}^*$ for the $\check{x}^*$ and $\check{y}^*$ directions, respectively. The effective density, capacitance[4] and thermal conductivity of nanofluid are defined as follows:

$$\check{\rho}_{nf} = (1-\phi)\,\rho_f + \phi\rho_s, \tag{5}$$

$$\left(\check{\rho}c_{\check{p}}\right)_{nf} = (1-\phi)\left(\rho c_p\right)_f + \phi\rho c_p, \tag{6}$$

$$\frac{\check{k}_{nf}}{\check{k}_f} = \frac{\check{k}_s + (n-1)\,\check{k}_f - \phi\,(n-1)\left(\check{k}_f - \check{k}_s\right)}{\check{k}_s + (n-1)\,\check{k}_f + \phi\left(\check{k}_f - \check{k}_s\right)}, \tag{7}$$

where $n = \frac{3}{\varpi}$ is the shape factor and ϖ is the sphericity of nanoparticles. Shape factors and thermophysical information are given in Tables 1 and 2, respectively.

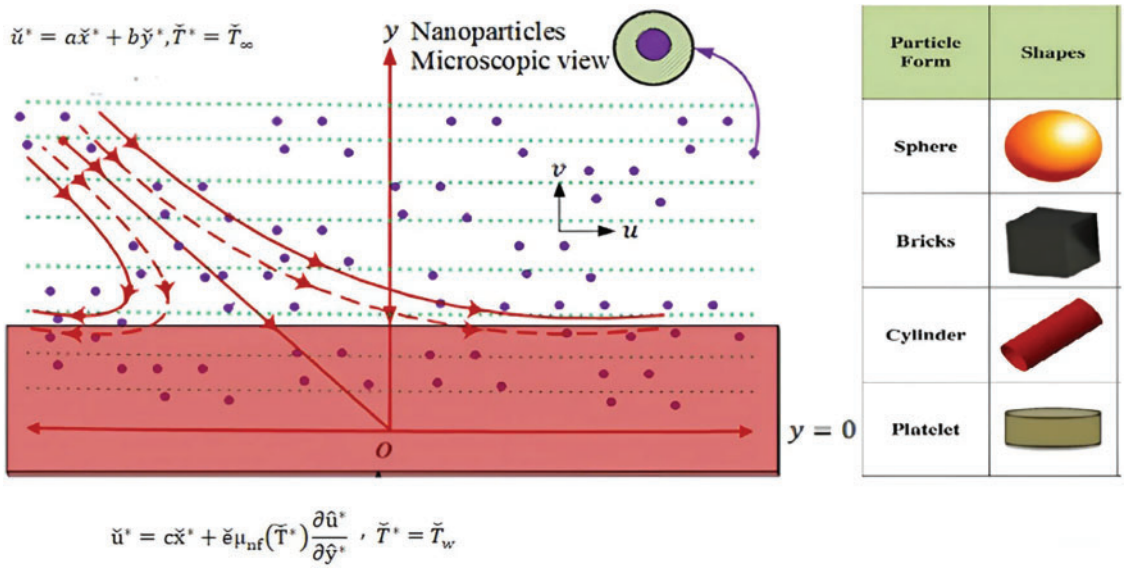

Figure 1: Physical description of the flow problem

Table 1: Shape factor for various shapes of GO nanoparticles

Shapes	*n*
Brick	3.7
Blade	8.6
Cylinder	4.8
Platelet	5.7
Spherical	3

Table 2: Properties of blood and GO nanoparticles

Properties	$\rho\,(\mathrm{kg.m^{-3}})$	$c_{\hat{p}}\,(\mathrm{J.kg^{-1}.K^{-1}})$	$k\,(\mathrm{W.m^{-1}.K^{-1}})$
Blood	1063	3594	0.492
Graphene oxide	1800	717	5000

Respective boundary conditions are [4]

$$\check{u}^* = c\check{x}^* + \check{e}\mu_{nf}\left(\check{T}^*\right)\frac{\partial \hat{u}^*}{\partial \hat{y}^*}, \check{v}^* = 0, \check{T}^* = \check{T}_w at \check{y}^* = 0, \tag{8}$$

$$\check{u}^* = a\check{x}^* + b\check{y}^*, \check{T}^* = \check{T}_\infty as \check{y}^* \to \infty. \tag{9}$$

Since the nanofluids are more likely to exhibit the slip condition at the stretching boundary, that is why the velocity slip condition is employed for accurately describing the velocity profile in the boundary layer. In Eq. (8), $c\check{x}^*$ is the velocity of the stretching surface, where c is the stretching rate. $c > 0$ indicates that the sheet is stretching, $c < 0$ implies a shrinking sheet and $c = 0$ is referred to as stationary surface. $\check{e}$ is the slip length and $\frac{\partial \hat{u}^*}{\partial \hat{y}^*}$ represents the velocity gradient near the boundary. $\check{T}_w$ and $\check{T}_\infty$ denote the temperature of the boundary and free stream temperature $(\check{T}_w > \check{T}_\infty)$. In Eq. (9), a and b are indicate the proportionality constants of free stream straining velocity and shear velocity. Introducing the following similarity transformations:

$$\check{x} = \check{x}^*\sqrt{\frac{c}{\nu_f}}, \check{y} = \check{y}^*\sqrt{\frac{c}{\nu_f}}, \check{u} = \check{u}^*\frac{1}{\sqrt{\nu_f c}}, \check{v} = \check{v}^*\frac{1}{\sqrt{\nu_f c}}, \check{p} = \frac{\check{p}^*}{(\rho\nu)_f c}, \check{T} = \frac{\check{T}^* - \check{T}_\infty}{\check{T}_w - \check{T}_\infty}, \tag{10}$$

where ν_f indicates the kinematic viscosity of carrier fluid (water).

Employing Eq. (10), in Eqs. (1)–(4) and (8), (9), their non-dimensional forms are

$$\frac{\partial \check{u}}{\partial \check{x}} + \frac{\partial \check{v}}{\partial \check{y}} = 0, \tag{11}$$

$$\check{u}\frac{\partial \check{u}}{\partial \check{x}} + \check{v}\frac{\partial \check{u}}{\partial \check{y}} + \frac{\rho_f}{\rho_{nf}}\frac{\partial \check{p}}{\partial \check{x}} = \frac{e^{-m\check{T}}}{\left(\left(1-\phi+\frac{\rho_s}{\rho_f}\phi\right)(1-\phi)^{2.5}\right)}\left(\frac{\partial^2 \check{u}}{\partial \check{y}^2} - m\frac{\partial \check{u}}{\partial \check{y}}\frac{\partial \check{T}}{\partial \check{y}}\right), \tag{12}$$

$$\check{u}\frac{\partial \check{v}}{\partial \check{x}} + \hat{v}\frac{\partial \check{v}}{\partial \check{y}} + \frac{\rho_f}{\rho_{nf}}\frac{\partial \check{p}}{\partial \check{y}} = \frac{e^{-m\check{T}}}{\left(\left(1-\phi+\frac{\rho_s}{\rho_f}\phi\right)(1-\phi)^{2.5}\right)}\left(\frac{\partial^2 \check{v}}{\partial \check{y}^2} - m\frac{\partial \check{v}}{\partial \check{y}}\frac{\partial \check{T}}{\partial \check{y}}\right), \tag{13}$$

$$\left(\check{u}\frac{\partial \check{T}}{\partial \check{x}} + \check{v}\frac{\partial \check{T}}{\partial \check{y}}\right) = \left(\frac{\alpha_{nf}}{\nu_f}\right)\frac{\partial^2 \check{T}}{\partial \check{y}^2}, \tag{14}$$

$$\check{u} = \check{x} + \frac{\omega e^{-m\check{T}}}{(1-\phi)^{2.5}}\frac{\partial \check{u}}{\partial \check{y}}, \check{v} = 0, \check{T} = 1at\check{y} = 0, \tag{15}$$

$$\check{u} = \frac{a}{c}\check{x} + \frac{b}{c}\check{y}, \check{T} = 0 \text{ when } \check{y} \to \infty, \tag{16}$$

where $m = d\left(T\check{w} - T\check{\infty}\right)$ is the viscosity variation coefficient, $\alpha_{nf} = \frac{k_{nf}}{(\rho c_{\hat{p}})_{nf}}$ is nanofluid's thermal conductivity, $\omega = \check{e}\check{\rho}_f\sqrt{\check{\nu}fc}$ signifies slip coefficient, $B = \frac{a}{c}$ is the stretching constant and $\gamma = \frac{b}{c}$ represents flow obliqueness coefficient. Initiating the streamline function relations [4] in Eqs. (11)–(16).

$$\check{u} = \frac{\partial \psi}{\partial \check{y}}, \check{v} = -\frac{\partial \psi}{\partial \check{x}}. \tag{17}$$

$$\frac{\partial \psi}{\partial \check{y}}\frac{\partial^2 \psi}{\partial \check{x}\partial \check{y}} - \frac{\partial \psi}{\partial \check{x}}\frac{\partial^2 \psi}{\partial \check{y}^2} + \frac{\rho_f}{\rho_{nf}}\frac{\partial \check{p}}{\partial \check{x}} = \frac{e^{-m\check{T}}}{\left(\left(1-\phi+\frac{\rho_s}{\rho_f}\phi\right)(1-\phi)^{2.5}\right)}\left(\frac{\partial^3 \psi}{\partial \check{y}^3} - m\frac{\partial^2 \psi}{\partial \check{y}^2}\frac{\partial \check{T}}{\partial \check{y}}\right), \tag{18}$$

$$-\frac{\partial \psi}{\partial \check{y}}\frac{\partial^2 \psi}{\partial \check{x}^2} + \frac{\partial \psi}{\partial \check{x}}\frac{\partial^2 \psi}{\partial \check{y}\partial \check{x}} + \frac{\rho_f}{\rho_{nf}}\frac{\partial \check{p}}{\partial \check{y}} = \frac{e^{-m\check{T}}}{\left(\left(1-\phi+\frac{\rho_s}{\rho_f}\phi\right)(1-\phi)^{2.5}\right)}\left(-\frac{\partial^3 \psi}{\partial \check{y}^2\partial \check{x}} + m\frac{\partial^2 \psi}{\partial \check{y}\partial \check{x}}\frac{\partial \check{T}}{\partial \check{y}}\right), \tag{19}$$

$$\left(\frac{\partial \psi}{\partial \check{y}}\frac{\partial \check{T}}{\partial \check{x}} - \frac{\partial \psi}{\partial \check{x}}\frac{\partial \check{T}}{\partial \check{y}}\right) = \left(\frac{\alpha_{nf}}{\nu_f}\right)\frac{\partial^2 \check{T}}{\partial \check{y}^2}, \tag{20}$$

$$\frac{\partial \psi}{\partial \check{y}} = \check{x} + \frac{\omega e^{-m\check{T}}}{(1-\phi)^{2.5}}\frac{\partial^2 \psi}{\partial \check{y}^2}, -\frac{\partial \psi}{\partial \check{x}} = 0, \check{T} = 1 \text{ at } \check{y} = 0, \tag{21}$$

$$\frac{\partial \psi}{\partial \check{y}} = \frac{a}{c}\check{x} + \frac{b}{c}\check{y}, \check{T} = 0 \text{ when } \check{y} \to \infty. \tag{22}$$

Differentiating Eq. (18) w.r.t $\check{y}$ and Eq. (19) w.r.t $\check{x}$

$$\begin{aligned}\frac{\partial \psi}{\partial \check{y}}\frac{\partial^3 \psi}{\partial \check{x}\partial \check{y}^2} - \frac{\partial \psi}{\partial \check{x}}\frac{\partial^3 \psi}{\partial \check{y}^3} + \frac{\rho_f}{\rho_{nf}}\frac{\partial^2 \check{p}}{\partial \check{y}\partial \check{x}} = \frac{e^{-m\check{T}}}{\left(\left(1-\phi+\frac{\rho_s}{\rho_f}\phi\right)(1-\phi)^{2.5}\right)}\left(-m\frac{\partial^3 \psi}{\partial \check{y}^3}\frac{\partial \check{T}}{\partial \check{y}} + m^2\frac{\partial^2 \psi}{\partial \check{y}^2}\left(\frac{\partial \check{T}}{\partial \check{y}}\right)^2 + \frac{\partial^4 \psi}{\partial \check{y}^4}\right.\\ \left. - m\frac{\partial^3 \psi}{\partial \check{y}^3}\frac{\partial \check{T}}{\partial \check{y}} - m\frac{\partial^2 \psi}{\partial \check{y}^2}\frac{\partial^2 \check{T}}{\partial \check{y}^2}\right),\end{aligned} \tag{23}$$

$$\begin{aligned}&-\frac{\partial^2 \psi}{\partial \check{x}\partial \check{y}}\frac{\partial^2 \psi}{\partial \check{x}^2} - \frac{\partial \psi}{\partial \check{y}}\frac{\partial^3 \psi}{\partial \check{x}^3} + \frac{\partial^2 \psi}{\partial \check{x}^2}\frac{\partial^2 \psi}{\partial \check{y}\partial \check{x}} + \frac{\partial \psi}{\partial \check{x}}\frac{\partial^3 \psi}{\partial \check{y}\partial \check{x}^2} + \frac{\rho_f}{\rho_{nf}}\frac{\partial^2 \check{p}}{\partial \check{x}\partial \check{y}}\\ &= \frac{e^{-m\check{T}}}{\left(\left(1-\phi+\frac{\rho_s}{\rho_f}\phi\right)(1-\phi)^{2.5}\right)}\left(m\frac{\partial^3 \psi}{\partial \check{y}^2\partial \check{x}}\frac{\partial \check{T}}{\partial \check{x}} + m\frac{\partial^2 \psi}{\partial \check{y}\partial \check{x}}\frac{\partial \check{T}}{\partial \check{y}}\frac{\partial \check{T}}{\partial \check{x}} - \frac{\partial^4 \psi}{\partial \check{y}^2\partial \check{x}^2}\right.\\ &\left. + m\frac{\partial^3 \psi}{\partial \check{y}\partial \check{x}^2}\frac{\partial \check{T}}{\partial \check{y}} + m\frac{\partial^2 \psi}{\partial \check{y}\partial \check{x}}\frac{\partial^2 \check{T}}{\partial \check{x}\partial \check{y}}\right).\end{aligned} \tag{24}$$

Subtracting Eqs. (23) from (24) and eliminating $\hat{p}$ using the certitude that $\check{p}_{\check{x}\check{y}} = \check{p}_{\check{y}\check{x}}$, we have

$$\begin{aligned}&\frac{e^{-\check{m}T}}{\left(\left(1-\phi+\frac{\rho_s}{\rho_f}\phi\right)(1-\phi)^{2.5}\right)}\left(-m\frac{\partial \check{T}}{\partial \check{y}}\frac{\partial}{\partial \check{y}}\left(\nabla^2\psi\right) + \frac{\partial^2}{\partial \check{y}^2}\left(\nabla^2\psi\right) + m^2\frac{\partial^2 \psi}{\partial \check{y}^2}\left(\frac{\partial \check{T}}{\partial \check{y}}\right)^2 - m\frac{\partial^3 \psi}{\partial \check{y}^3}\frac{\partial \check{T}}{\partial \check{y}} - m\frac{\partial^2 \check{T}}{\partial \check{y}^2}\frac{\partial^2 \psi}{\partial \check{y}^2}\right.\\ &\left. - m\frac{\partial \check{T}}{\partial \check{x}}\frac{\partial^3 \psi}{\partial \check{y}^2\partial \check{x}} + m^2\frac{\partial \check{T}}{\partial \check{x}}\frac{\partial^2 \psi}{\partial \check{y}\partial \check{x}}\frac{\partial \check{T}}{\partial \check{y}} - m\frac{\partial^2 \psi}{\partial \check{y}\partial \check{x}}\frac{\partial^2 \check{T}}{\partial \check{y}\partial \check{x}}\right) + \frac{\partial\left(\psi, \nabla^2\psi\right)}{\partial\left(\check{x}, \check{y}\right)} = 0.\end{aligned} \tag{25}$$

Revising the stream function as $\psi(\check{x},\check{y}) = \check{x}F(\check{y}) + G(\check{y})$, $\check{T}(\check{x},\check{y}) = \theta(\check{y})$, in Eqs. (25), (20)–(22) and comparing coefficients we get

$$\frac{e^{-m\theta}}{\left(\left(1-\phi+\frac{\rho_s}{\rho_f}\phi\right)(1-\phi)^{2.5}\right)}\left(-m\theta' F''' + F^{iv} + m^2 F''\theta'^2 - mF'''\theta' - m\theta'' F''\right) - F'F'' + FF''' = 0, \tag{26}$$

$$\frac{e^{-m\theta}}{\left(\left(1-\phi+\frac{\rho_s}{\rho_f}\phi\right)(1-\phi)^{2.5}\right)}\left(-m\theta' G''' + G^{iv} + m^2 G''\theta'^2 - mG'''\theta' - m\theta'' G''\right) - F''G' + FG''' = 0, \tag{27}$$

$$\left(\frac{k_{nf}}{k_f}\right)\theta'' + Pr\left(1-\phi+\frac{(\rho c_{\check{p}})_s}{(\rho c_{\check{p}})_f}\phi\right)F\theta' = 0, \tag{28}$$

$$\check{x}F'(y) + G'(y) = \check{x} + \frac{\omega e^{-m\check{T}}}{(1-\phi)^{2.5}}(\check{x}F''(y) + G''(y)), F'(y) = 0, \theta(\check{y}) = 1 \text{ at } \check{y} = 0, \tag{29}$$

$$\check{x}F'(y) + G'(y) = \frac{a}{c}\check{x} + \frac{b}{c}\check{y}, \theta(\check{y}) = 0 \text{ when } \check{y} \to \infty, \tag{30}$$

where k_{nf} stands for heat transfer coefficient of nanofluid and $Pr = \frac{\nu_f}{\alpha_f}$ signifies the Prandtl number. Above surface conditions eventually become

$$F(0) = 0, F'(0) = 1 + \frac{\omega e^{-m\theta(0)}}{(1-\phi)^{2.5}}F''(0), G'(0) = \frac{\omega e^{-m\theta(0)}}{(1-\phi)^{2.5}}G''(0), F'(\infty) = \frac{a}{c}, G''(\infty) = \gamma,$$
$$\theta(0) = 1, \theta(\infty) = 0. \tag{31}$$

where $F(\check{y})$ and $G(\check{y})$ are perpendicular and longitudinal flow component. Integrating Eqs. (26) and (27) once w.r.t $\check{y}$

$$\frac{e^{-m\theta}}{\left(\left(1-\phi+\frac{\rho_s}{\rho_f}\phi\right)(1-\phi)^{2.5}\right)}\left(F''' - m\theta' F''\right) + FF'' - (F')^2 + K_1 = 0, \tag{32}$$

$$\frac{e^{-m\theta}}{\left(\left(1-\phi+\frac{\rho_s}{\rho_f}\phi\right)(1-\phi)^{2.5}\right)}\left(G''' - m\theta' G''\right) + FG'' - F'G' + K_2 = 0. \tag{33}$$

Here K_1 and K_2 are arbitrary parameters and primes denote the differential coefficients w.r.t $\check{y}$. Applying limit $\check{y} \to \infty$on Eq. (32) and by means of condition $F'(\infty) = \frac{a}{c}$, we get $K_1 = \left(\frac{a}{c}\right)^2$. A boundary layer assessment of Eq. (32) specifies that $F(\check{y}) = \left(\frac{a}{c}\right)\check{y} + A$ when $\check{y} \to \infty$, where constant A denotes surface layer displacement. Taking limit $\check{y} \to \infty$ on Eq. (33) and applying constraints at $G''(\infty) = \gamma$, we get $K_2 = -A\gamma$. Thus Eqs. (32) and (33) become

$$(1-\phi)^{-2.5}e^{-m\theta}\left(F''' - m\theta' F''\right) + \left(1-\phi+\frac{\rho_s}{\rho_f}\phi\right)\left(F''F - (F')^2 + \left(\frac{a}{c}\right)^2\right) = 0, \tag{34}$$

$$(1-\phi)^{-2.5} e^{-m\theta} \left(G''' - m\theta' G''\right) + \left(1 - \phi + \frac{\rho_s}{\rho_f}\phi\right)\left(G''F - G'F' - A\gamma\right) = 0. \tag{35}$$

Introducing

$$G'\left(\check{y}\right) = \gamma H\left(\check{y}\right). \tag{36}$$

Using Eqs. (36) in (35) and surface conditions in (31)

$$(1-\phi)^{-2.5} e^{-m\theta} \left(H'' - m\theta' H'\right) + \left(1 - \phi + \frac{\rho_s}{\rho_f}\phi\right)\left(H'F - HF' - A\right) = 0, \tag{37}$$

$$H\left(0\right) = \frac{\omega e^{-m\theta(0)}}{\left(1-\phi\right)^{2.5}} H'\left(0\right), H'\left(\infty\right) = 1. \tag{38}$$

$$\check{T}_w^* = \left[\mu_{nf}\left(\check{T}^*\right)\frac{\partial \check{u}^*}{\partial \check{y}^*}\right]_{\check{y}^*=0}, \tag{39}$$

$$\check{Q}_\omega^* = -\check{k}_{nf}\left(\frac{\partial \check{T}^*}{\partial \check{y}^*}\right)_{\check{y}^*=0}. \tag{40}$$

Prominent system variables such as shearing force and thermal flux at the extended surface in dimensionless form are

$$\check{T}_\omega = \frac{e^{-m\theta(0)}}{\left(1-\phi\right)^{2.5}}\left(\check{x}F''\left(0\right) + \gamma H'(0)\right), \tag{41}$$

$$\check{Q}_\omega = -\left(\frac{\check{k}_{nf}}{\check{k}_f}\right)\theta'\left(0\right). \tag{42}$$

Stagnation point is given by

$$\check{x} = -\frac{\gamma H'\left(0\right)}{F''\left(0\right)}. \tag{43}$$

3 Numerical Solution

The final boundary value problem is represented by a system of three ODEs (ordinary differential equations) of total order seven: Eq. (34) (third-order normal momentum), Eq. (37) (reduced second-order tangential momentum), and Eq. (28) (second-order temperature), along with their boundary conditions from Eq. (31) modified by the replacement conditions in Eq. (38). Solving this system analytically is extremely challenging, if not entirely unfeasible. Therefore, a computational approach is adopted, using numerical quadrature (specifically, a shooting algorithm) combined with the robust Runge-Kutta Fehlberg method. The approximate CPU time for this execution is 10^{-1} s. Various schemes [41–43] are available to solve fluid flow problems but this approach can easily handle multi-order ordinary differential boundary value problems (BVPs) and has been implemented in various studies using different symbolic codes. Its main advantage is its stability when applied to stiff equations. This method [44] uses an efficient procedure to determine an appropriate step size of h = 0.0001 for stepping. Two different approximations are made for the solution and compared, with the step size being considered acceptable if the results are in strong agreement.

Otherwise, the process is repeated with a smaller step size. Following six values are required in each step:

$$I_1 = hf\left(t_k, y_k\right),$$

$$I_2 = hf\left(t_k + \frac{1}{4}h, y_k + \frac{1}{4}I_1\right),$$

$$I_3 = hf\left(t_k + \frac{3}{8}h, y_k + \frac{3}{32}I_1 + \frac{9}{32}I_2\right),$$

$$I_4 = hf\left(t_k + \frac{12}{13}h, y_k + \frac{1932}{2197}I_1 - \frac{7200}{2197}I_2 + \frac{7296}{2197}I_3\right),$$

$$I_5 = hf\left(t_k + h, y_k + \frac{439}{216}I_1 - 8l_2 + \frac{3680}{513}I_3 - \frac{845}{4104}I_4\right),$$

$$I_6 = hf\left(t_k + \frac{1}{2}h, y_k - \frac{8}{27}I_1 + 2I_2 - \frac{3544}{2565}I_3 + \frac{1859}{4104}I_4 - \frac{11}{40}I_5\right).$$

Using RK 4th order scheme, the I.V.P is approximated as

$$y_{k+1} = y_k + \frac{25}{216}I_1 + \frac{1408}{2565}I_3 + \frac{2197}{4104}I_4 - \frac{1}{5}I_5. \tag{44}$$

By applying the following substitutions in Eqs. (25), (27), and (30), the final system of three coupled ordinary differential equations of total order seven, along with the modified boundary conditions in (26) and (31), is obtained.

$$\left.\begin{pmatrix} F \\ F' \\ F'' \end{pmatrix} = \begin{pmatrix} y_1 \\ y_1' = y_2 \\ y_2' = y_3 \end{pmatrix}, \begin{pmatrix} H \\ H' \\ \theta \\ \theta' \end{pmatrix} = \begin{pmatrix} y_4 \\ y_4' = y_5 \\ y_5' = y_6 \\ y_6' = y_7 \end{pmatrix}\right\}. \tag{45}$$

The following system of differential equations, which defines the transformed three flow variables (the two linear velocity components and temperature), is then derived:

$$\begin{pmatrix} y_3' \\ y_5' \\ y_7' \end{pmatrix} = \begin{pmatrix} my_7y_3 - \xi e^{my_6}\left(y_1y_3 - {y_2}^2 + \left(\frac{a}{c}\right)^2\right) \\ my_7y_5 - \xi e^{my_6}\left(y_1y_5 - y_2y_4 - A\right) \\ -Pr\left(\frac{k_f}{k_{nf}}\right)\left(1 - \phi + \frac{\left(\rho c_{\hat{p}}\right)_s}{\left(\rho c_{\hat{p}}\right)_f}\phi\right)y_1y_7 \end{pmatrix}, \tag{46}$$

where $\xi = \left(1 - \phi + \frac{\rho_s}{\rho_f}\phi\right)(1-\phi)^{2.5}$, the finalized numerical boundary conditions become

$$y_1 = 0,\ y_2 = 1,\ y_3 = b_1,\ y_4 = 0,\ y_5 = b_2,\ y_6 = 1,\ y_7 = b_3 \text{ at } 0. \tag{47}$$

Here $b_1, b_2,$ and b_3 are initial guesses for the shooting parameters, which are then refined using Newton-Raphson's method for each set of parameter values based on the specified free stream conditions.

4 Results and Discussion

The primary goal of this study is to assess the thermal performance of a nanofluid (GO-Blood) under the influence of different factors, including the shape factor of nanoparticles and the temperature-dependent viscosity parameter, stretching ratio parameter and velocity slip parameter. The nanofluid is composed of Graphene oxide dispersed in a base liquid blood. The study examines how the enhanced thermal (physical) properties of the nanofluid influence the velocity and temperature distributions within the fluid, as well as the friction drag coefficient and heat transfer rate. The graphical results achieved by the numerical scheme are presented through Figs. 2 to 18. Nanoparticle concentration is considered 5%, and Prandtl number of blood is taken $Pr = 21$. Fig. 2 depicts the normal component of velocity for different shapes of graphene oxide nanoparticles. Graphical outcomes revealed that the highest velocity is achieved for spherical shape, whereas it is the minimum for platelet shape. The shape factor indicates that platelet shape has higher thermal conductivity than spherical shape. The reason behind this trend is that nanoparticles with lower thermal conductivity impede heat transfer, resulting in thicker thermal boundary layers and requiring a higher normal velocity to overcome the added resistance. On the other hand, nanoparticles with higher thermal conductivity enhance heat dissipation, this results in thinner thermal boundary layer and a lower normal velocity. Fig. 3 is plotted to study the influence of nanoparticles shapes upon tangential component of oblique blood based nanofluid flow. An opposite trend of $\boldsymbol{H'(y)}$ under the influence of shape factor can be witnessed closer to the surface, conversely away from the surface it has same behavior as $\boldsymbol{F'(y)}$. The tangential velocity refers to the flow component that runs parallel to the surface. It is primarily affected by the shear stress at the wall and the frictional resistance within the boundary layer. The shape of the nanoparticles plays a key role in influencing the flow resistance in this direction as well. Platelet shape nanoparticles generate less shear stresses at the surface, which leads to lesser frictional resistance in the tangential direction. This decreases the resistance to tangential flow and results in a higher tangential velocity. Fig. 4 represents the effect of shapes of nanoparticles on temperature distribution within the nanofluid flow. It is very obvious that temperature tends to boost for platelet shape nanoparticles due to higher thermal conductivity on the other hand the lowest distribution is observed for spherical shape because of lowest thermal conductivity.

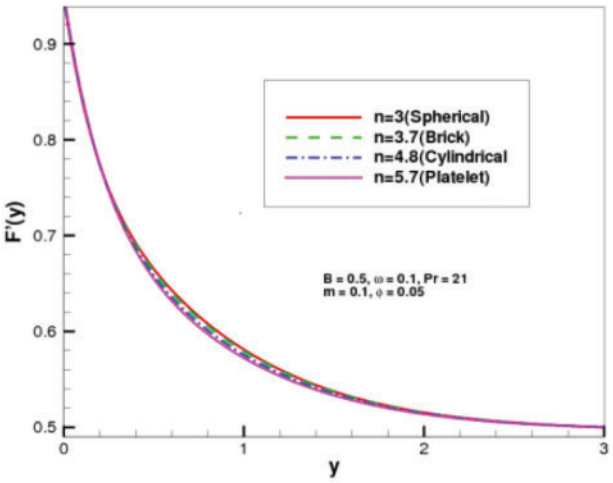

Figure 2: $F'(y)$ vs. different shapes of nanoparticles

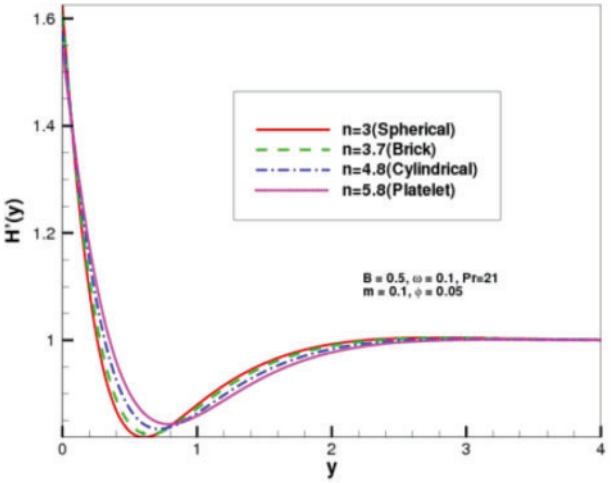

Figure 3: $H'(y)$ vs. different shapes of nanoparticles

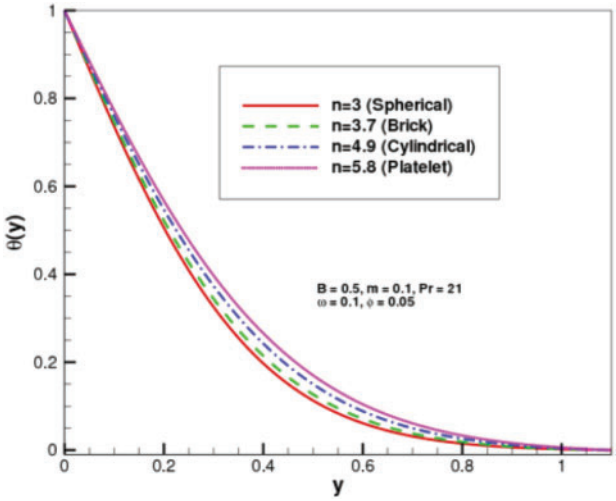

Figure 4: $\theta(y)$ vs. different shapes of nanoparticles

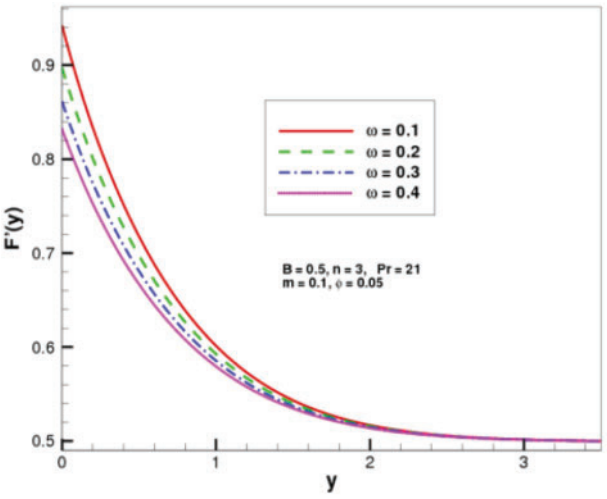

Figure 5: $F'(y)$ vs. slip parameter ω

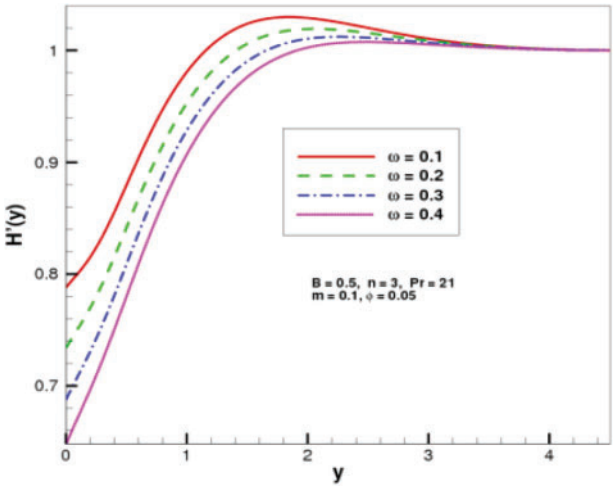

Figure 6: $H'(y)$ vs. slip parameter ω

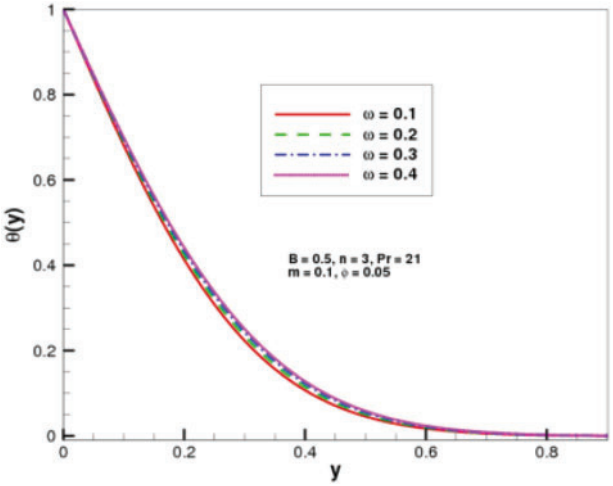

Figure 7: $\theta(y)$ vs. slip parameter $\boldsymbol{\omega}$

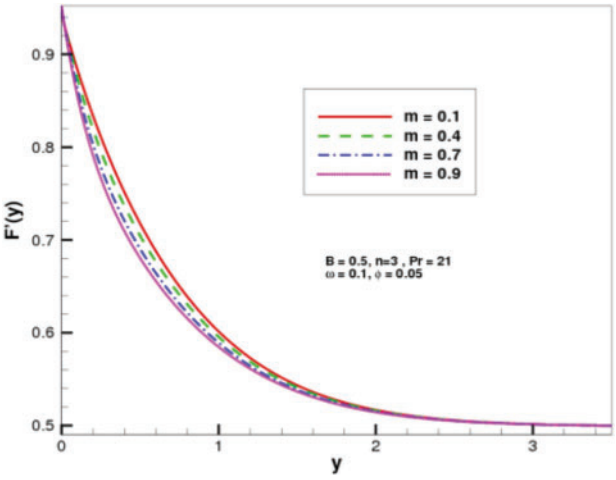

Figure 8: $F'(y)$ vs. viscosity parameter m

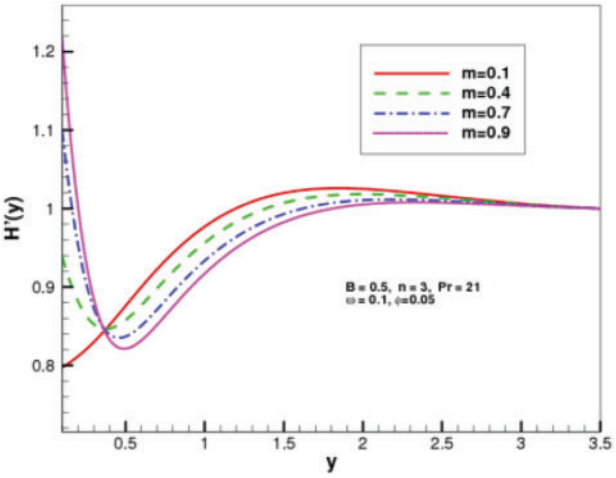

Figure 9: $H'(y)$ vs. viscosity parameter m

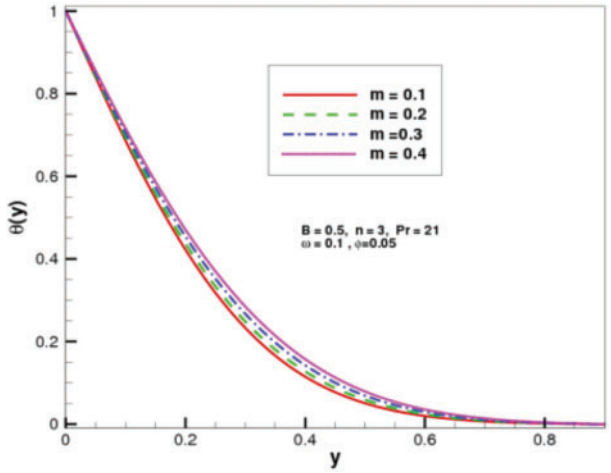

Figure 10: $\theta(y)$ vs. viscosity parameter m

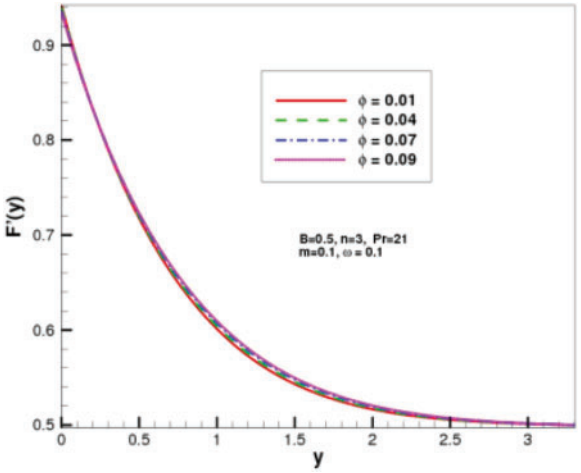

Figure 11: $F'(y)$ vs. nanoparticles volume fraction(ϕ)

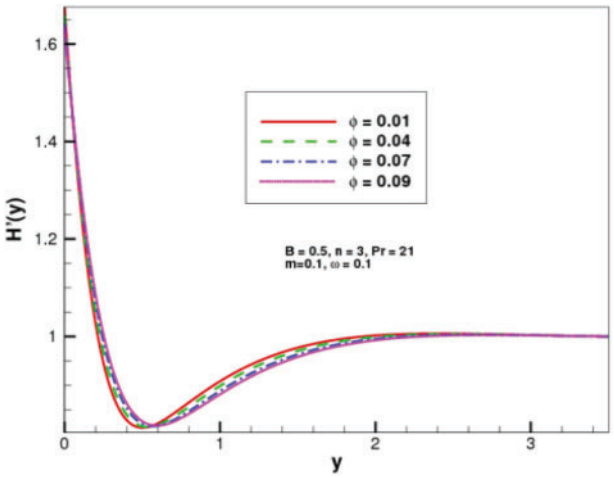

Figure 12: $H'(y)$ vs. nanoparticles volume fraction(ϕ)

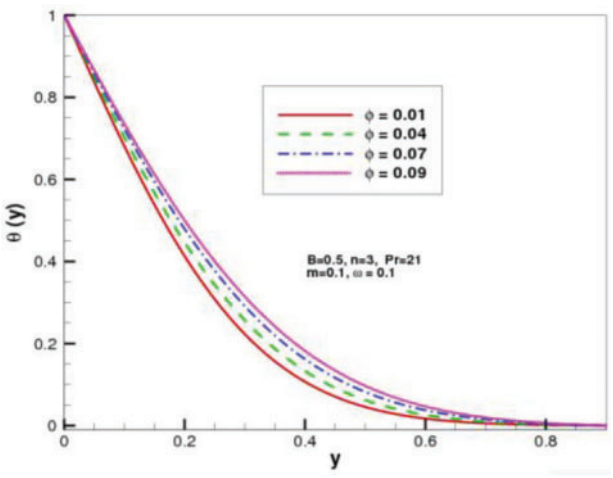

Figure 13: $\theta(y)$ vs. nanoparticles volume fraction (ϕ)

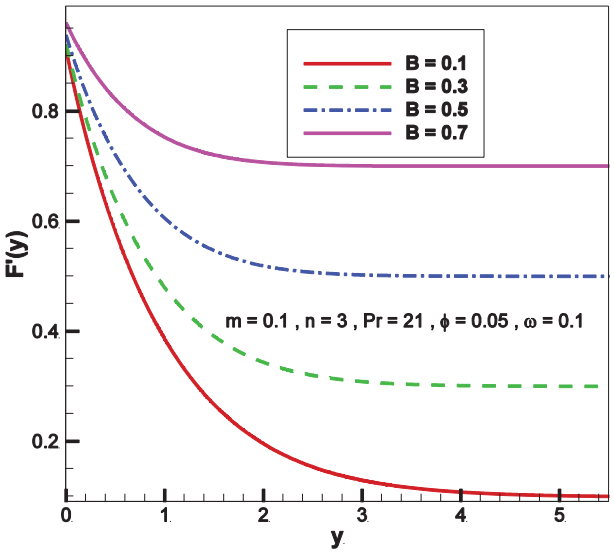

Figure 14: $F'(y)$ vs. stretching ratio parameter B

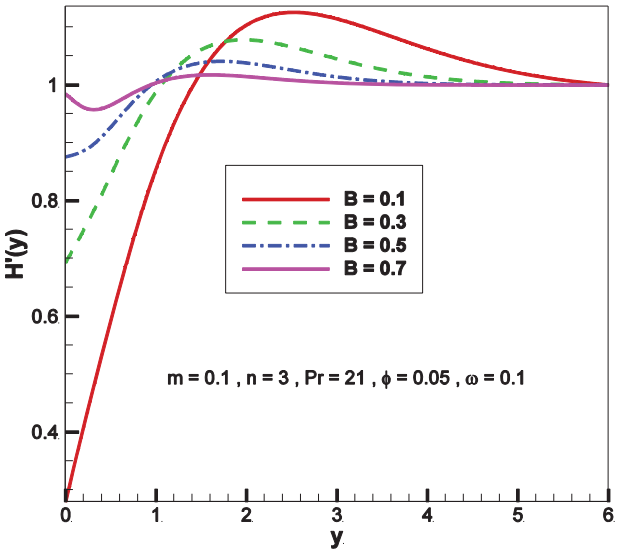

Figure 15: $H'(y)$ vs. stretching ratio parameter B

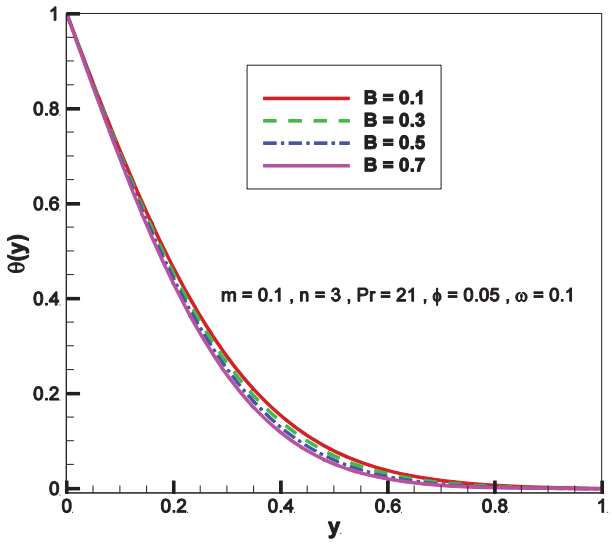

Figure 16: $\theta(y)$ vs. stretching ratio parameter B

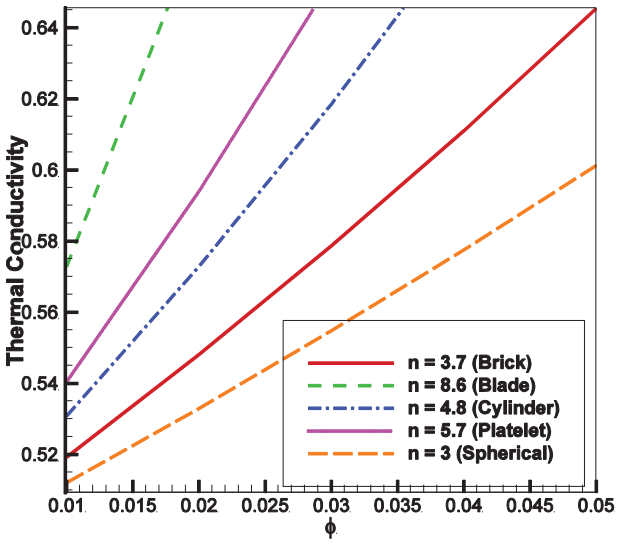

Figure 17: Impact of various shapes of nanoparticles on thermal conductivity of nanofluid

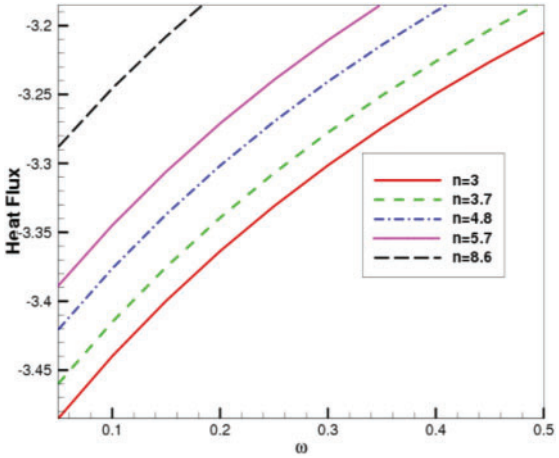

Figure 18: Heat transfer rate when varying the nanoparticles shapes

Figs. 5 and 6 are presented to examine the effect of the velocity slip parameter on both velocity profiles. The graphs indicate that an increase in the slip parameter ωleads to a decrease in both velocity profiles, $F'(y)$ and $\boldsymbol{H'(y)}$. The velocity slip parameter represents the difference in velocity between the fluid and the solid surface at the boundary, enabling a "slip" effect at the surface. This slip occurs when the no-slip condition, which assumes the fluid velocity at the surface is zero, is relaxed. Typically, the slip velocity is modeled as being proportional to the velocity gradient at the boundary. The velocity slip parameter affects both the perpendicular and longitudinal velocity profiles of non-aligned flow towards the stagnation point by modifying the interaction between the fluid and the surface, as well as the overall flow resistance. As the velocity slip parameter increases, the resistance to normal flow near the surface decreases, and the fluid is able to slip more easily. This results in reduced viscous drag in the normal direction. Consequently, the normal velocity decreases because the fluid no longer needs to accelerate as much in the normal direction to overcome wall resistance. The tangential velocity, which is the flow component parallel to the surface, is

influenced by the shear stress at the surface. The velocity slip parameter affects the shear stress, which in turn impacts the **tangential velocity** and reducing the need for the fluid to accelerate as much in the tangential direction. Fig. 7 shows that increase in slip coefficient enhances the temperature distribution $\boldsymbol{\theta}(\boldsymbol{y})$. As the slip parameter increases, the fluid near the surface can move more freely, reducing the energy needed to overcome frictional forces. This allows for more efficient heat transport rate from the surface to the fluid. As a result, the heat transfer rate increases, leading to a rise in the temperature of the fluid close to the surface.

Figs. 8 and 9 are plotted to inspect the influence of viscosity variation parameter m upon normal $F'(y)$ and tangential velocity $H'(y)$ outlines. It can be seen that $F'(y)$ declines, on the other hand $H'(y)$ increases with m. When viscosity decreases, the fluid near the surface can accelerate more easily. In oblique stagnation point flow, the normal velocity contributes to the component of the flow directed towards the surface. As viscosity lowers, the velocity gradients near the surface become less steep, allowing the fluid to adjust more quickly to the no-slip boundary condition. This results in a reduction in the normal velocity component near the surface. The tangential velocity, which is parallel to the surface, is less directly influenced by the no-slip condition (it doesn't have to be zero at the surface, though it typically decreases there). With lower viscosity, the fluid faces less resistance to shear stress, enabling the tangential velocity to increase near the surface. Furthermore, as the normal velocity decreases, the tangential velocity compensates by increasing in order to maintain the overall momentum balance in the flow. This leads to an increase in the tangential velocity profile near the surface.

Fig. 10 shows that growing values of m augments the thermal distribution within the nanofluid flux. As the viscosity parameter upsurges, the fluid encounters less resistance to flow, causing the velocity boundary layer to become thinner. This facilitates more efficient heat transport from the surface to the fluid. As a result, the increased heat transfer raises the local temperature within the thermal boundary layer, leading to a higher temperature profile near the surface. Figs. 11 and 12 reveal that nanoparticles volume fraction has increasing trend on normal velocity profile, similarly it has the same trend on circumferential velocity adjacent to the surface but distant from the surface this trend reverses. A rise in nanoparticle's volume fraction results in higher perpendicular and longitudinal velocity profiles in oblique flows, driven by several factors.

These include enhanced heat transfer, improved momentum transfer by the nanoparticles, possible reductions in flow resistance (depending on changes in viscosity), and alterations to the boundary layer thickness. Together, these effects facilitate more efficient fluid motion, leading to an increase in both velocity components near the surface. Fig. 13 is indicating in increasing trend in temperature distribution with respect to nanoparticles volume fraction ϕ. It is because of the rise in thermal conductivity for higher value of ϕ. Figs. 14 and 15 are generated to focus on impact of stretching ratio constant $\boldsymbol{B} = \frac{\boldsymbol{a}}{\boldsymbol{c}}$ upon flow characteristics, which is the ratio of free stream constant $\boldsymbol{a}$ to the stretching surface constant $\boldsymbol{c}$. Increase in $\boldsymbol{B}$ indicates higher free stream straining velocity as compare to the velocity of stretching surface. This trend causes the enhancement in both of the velocity outlines $\boldsymbol{F'(y)}$ and $\boldsymbol{H'(y)}$. Fig. 16 Increasing the stretching parameter leads to a reduction in temperature due to enhanced nanofluid velocity which consequently declines the temperature distribution. Table 3 is presented to study the how the nanoparticle volume fraction of different shapes influences the thermal conductivity. It is evident that blade shape nanoparticles have highest thermal conductivity that increases rapidly w.r.t ϕ, whereas lowest conductivity is achieved with spherical shape. This behavior is graphically shown through Fig. 17. Fig. 18 is depicting a direct relationship between heat flux and nanoparticles shape and slip paramter. It is observed that heat transport rate grows with slip parameter and maximum heat flux is gained with blade shape due to its highest thermal conductivity. In Figs. 19 and 20, normal skin friction has increasing trend with respect to slip parameter and the decreasing with respect to GO volume fraction. Tangential Skin friction has opposite trend to the normal skin friction.

It is also noted that perpendicular drag component declines and longitudinal component rises with higher values of GO nanoparticles.

Table 3: Effective thermal conductivity of nanofluid w.r.t various nanoparticle shapes

n/ϕ	**0.01**	**0.02**	**0.03**	**0.04**	**0.05**
3.7 (Brick)	0.5192950272	0.5481475219	0.5786947042	0.6110904006	0.6455076363
8.6 (Blade)	0.5728610017	0.6682015055	0.7822931583	0.9212711176	1.094274647
4.8 (Cylinder)	0.5308499466	0.5728937104	0.6185420156	0.6682791645	0.7226802893
5.7 (Platelet)	0.5405003090	0.5940295453	0.6534126403	0.7196653873	0.7940530299
3 (Spherical)	0.5120755849	0.5329873950	0.5547887903	0.5775377682	0.6012974803

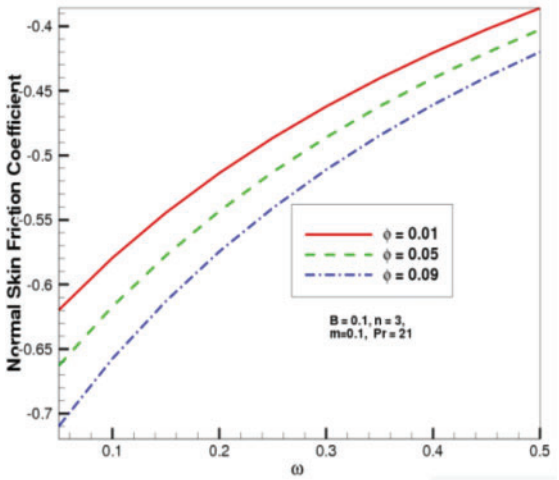

Figure 19: Normal component of skin friction for (ϕ)

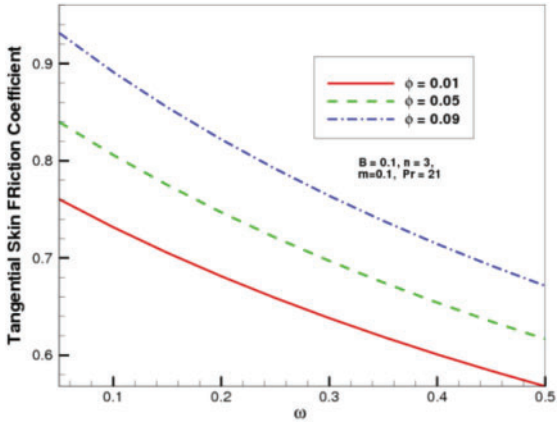

Figure 20: Tangential component of skin friction for (ϕ)

The normal skin friction coefficient represents the resistance the fluid experiences in the direction perpendicular to the surface at the stagnation point. As the nanoparticle volume fraction rises, the fluid's

effective viscosity increases, which tends to lessen the velocity gradients near the surface in the normal direction. This increased viscosity results in a smoother transition in velocity perpendicular to the surface, thereby reducing the resistance in the normal direction. Tangential skin friction refers to the resistance in the direction parallel to the surface. As the nanoparticle concentration increases, the fluid's viscosity rises, which can enhance the shear stress near the surface. Higher viscosity generally results in a thicker boundary layer, leading to greater tangential friction, as the fluid's velocity within the boundary layer encounters more resistance. Streamline patterns for stretching ratio parameter B and viscosity parameter m with obliqueness parameter $\gamma = 1$ are presented through Figs. 21 and 22. Streamlines for smaller stretching ratio parameter are more tilted towards left as compare to streamlines for higher stretching ratio constant. Similarly streamline of nanofluid with variable viscosity are more oblique towards left than streamlines with constant viscosity.

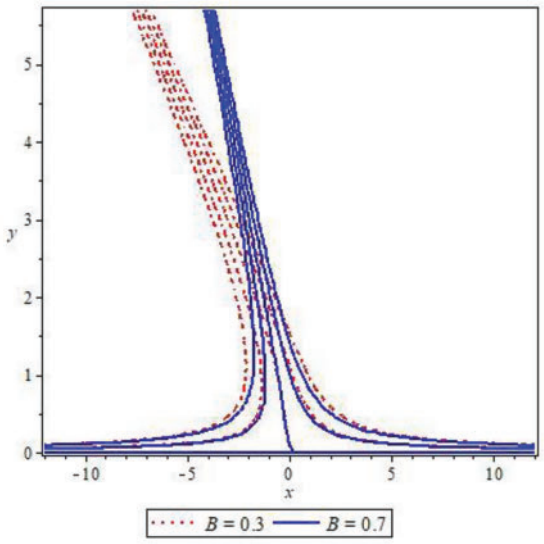

Figure 21: Streamlines for stretching ratio constant B

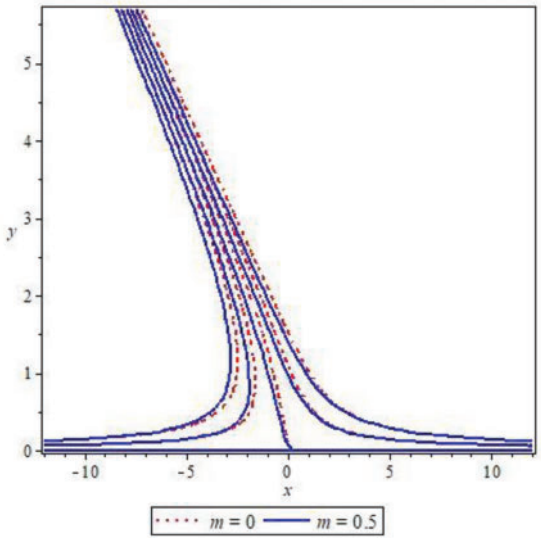

Figure 22: Streamlines for constant and variable viscosity

5 Concluding Remarks

A blood-based non-aligned stagnation point flow with graphene oxide nanoparticles has been studied under the influence of various shapes of nanoparticles. The numerical outcomes of the governing equations are:

- The normal velocity profile is showing maximum velocity with spherical and the minimum velocity with platelet shape of nanoparticles. $H'(y)$ is increasing near the surface and is showing the same behavior as normal velocity away from the surface.
- Maximum temperature distribution is achieved with blade shape. It is also seen that the temperature profile enhanced significantly by increasing nanoparticle volume fraction from 1% to 9%.
- The effects of increasing the slip parameter ω on fluid dynamics. As ω rises, the velocity distribution $F'(y)$ shows a decline due to surged viscosity, resulting in stagnation flow deceleration. Similarly, the oblique velocity component $H'(y)$ declines with higher ω. Additionally, heightened slip parameters lead to increased opposition between the interface and fluid, causing an augmentation in heat interface layer thickness and heat transfer $\theta(y)$.
- Variable viscosity varies directly with viscous fluid and inversely with normal velocity. $H'(y)$ decreases near the surface when variable viscosity increases and *vice versa*, where m is proportional to the difference between temperatures. An increase in m indicates an increase in temperature.
- Nanoparticle volume fraction has an increasing effect on heat flux, and the highest thermal conductivity is achieved for blade-shaped nanoparticles.
- The normal drag coefficient has an increasing trend and the longitudinal friction coefficient has a decreasing trend with respect to the slip parameter.
- Streamline patterns are more inclined towards left for the stretching ratio parameter $B = 0.7$, similarly for the case of variable viscosity $m = 0.5$ same behavior is observed.

While this study offers important insights into heat transfer enhancement in blood-based oblique nanofluid flow by varying nanoparticle shapes and fluid viscosity concerning temperature, exploring the effects of unsteady (time-dependent) nanofluid flow under the assumptions made in this study would be an intriguing direction for future research.

Acknowledgement: The authors would like to thank Prince Sultan University, Saudi Arabia, for the technical support through the TAS Research Lab.

Funding Statement: The authors received no specific funding for this study.

Author Contributions: Rabil Tabassum: Modeling, methodology, manuscript preparation, supervision and review. M. Kamran: Literature review, methodology and graphical results. Khalil Ur Rehman: Validation, interpretation of results and review. Wasfi Shatanawi: Writing—review and editing. Rashid Mehmood: Review and editing. All authors reviewed the results and approved the final version of the manuscript.

Availability of Data and Materials: The data that support the findings of this study are available from the corresponding author upon reasonable request.

Ethics Approval: Not applicable.

Conflicts of Interest: The authors declare no conflicts of interest to report regarding the present study.

Nomenclature

$\check{u}$ $\hat{x}$-Component of velocity $\left(\mathrm{m.s}^{-1}\right)$
$\check{v}$ $\hat{y}$-Component of velocity $\left(\mathrm{m.s}^{-1}\right)$

$\check{T}$ Temperature (K)
$\check{T}_\infty$ Ambient temperature (K)
$\check{T}_w$ Wall temperature (K)
d Viscosity variation exponent
m Variable viscosity parameter
$\check{p}$ Pressure $\left(\mathrm{N.m^{-2}}\right)$
$\check{x}$ Cartesian coordinates along the stretching surface (m)
$\check{y}$ Cartesian coordinates normal to stretching surface (m)
$c_{\check{p}}$ Specific heat $\left(\mathrm{J.kg^{-1}.K^{-1}}\right)$
k Thermal conductivity $\left(\mathrm{W.m^{-1}.K^{-1}}\right)$
Pr Prandtl number

Greek Symbols

ϕ Solid volume fraction of nanoparticles
μ_0 Reference viscosity $\left(\mathrm{kg.m^{-1}.s^{-1}}\right)$
ν Kinematics viscosity $\left(\mathrm{m^2.s^{-1}}\right)$
ρ Density $\left(\mathrm{kg.m^{-3}}\right)$
α Thermal diffusivity $\left(\mathrm{m^2.s^{-1}}\right)$
γ Obliqueness of the flow
μ Dynamic viscosity $\left(\mathrm{kg.m^{-1}.s^{-1}}\right)$
ω Velocity slip parameter

Subscripts

f Base fluid
s Nanoparticles
nf Nanofluid

References

1. Jang SP, Choi SUS. Effects of various parameters on nanofluid thermal conductivity. J Heat Transf. 2007;129(5):617–23. doi:10.1115/1.2712475.
2. Li Y, Zhou JE, Tung S, Schneider E, Xi S. A review on development of nanofluid preparation and characterization. Powder Technol. 2009;196(2):89–101. doi:10.1016/j.powtec.2009.07.025.
3. Aybar HŞ, Sharifpur M, Azizian MR, Mehrabi M, Meyer JP. A review of thermal conductivity models for nanofluids. Heat Transf Eng. 2015;36(13):1085–110. doi:10.1080/01457632.2015.987586.
4. Tabassum R, Mehmood R, Pourmehran O, Akbar N, Gorji-Bandpy M. Impact of viscosity variation on oblique flow of Cu-H_2O nanofluid. J Process Mech Eng. 2018;232(5):622–31. doi:10.1177/0954408917732759.
5. Arshad A, Jabbal M, Yan Y, Reay D. A review on graphene based nanofluids: preparation, characterization and applications. J Mol Liq. 2019;279:444–84. doi:10.1016/j.molliq.2019.01.153.
6. Hatami M, Jing D. Introduction to nanofluids. In: Nanofluids. Amsterdam: Elsevier; 2020. p. 1–50. doi: 10.1016/b978-0-08-102933-6.00001-9.
7. Hatami M, Jing D. Nanofluid analysis in different applications. In: Nanofluids. Amsterdam: Elsevier; 2020. p. 283–347. doi:10.1016/b978-0-08-102933-6.00006-8.
8. Li J, Zhang X, Xu B, Yuan M. Nanofluid research and applications: a review. Int Commun Heat Mass Transf. 2021;127:105543. doi:10.1016/j.icheatmasstransfer.2021.105543.
9. Reza M, Gupta AS. Steady two-dimensional oblique stagnation-point flow towards a stretching surface. Fluid Dyn Res. 2005;37(5):334–40. doi:10.1016/j.fluiddyn.2005.07.001.
10. Mahapatra TR, Dholey S, Gupta AS. Oblique stagnation-point flow of an incompressible visco-elastic fluid towards a stretching surface. Int J Non Linear Mech. 2007;42(3):484–99. doi:10.1016/j.ijnonlinmec.2007.01.008.
11. Li D, Labropulu F, Pop I. Oblique stagnation-point flow of a viscoelastic fluid with heat transfer. Int J Non Linear Mech. 2009;44(10):1024–30. doi:10.1016/j.ijnonlinmec.2009.07.007.

12. Ishak A, Jafar K, Nazar R, Pop I. MHD stagnation point flow towards a stretching sheet. Phys A Stat Mech Appl. 2009;388(17):3377–83. doi:10.1016/j.physa.2009.05.026.
13. Mustafa M, Hayat T, Pop I, Asghar S, Obaidat S. Stagnation-point flow of a nanofluid towards a stretching sheet. Int J Heat Mass Transf. 2011;54(25–26):5588–94. doi:10.1016/j.ijheatmasstransfer.2011.07.021.
14. Ghaffar A. Oblique stagnation point flows [master's theses]. Regina, SK, Canada: Faculty of Graduate Studies and Research, University of Regina; 2012.
15. Lok YY, Merkin JH, Pop I. MHD oblique stagnation-point flow towards a stretching/shrinking surface. Meccanica. 2015;50(12):2949–61. doi:10.1007/s11012-015-0188-y.
16. Ghaffari A, Javed T, Mustafa I. Non-linear radiation influence on oblique stagnation point flow of Maxwell fluid. Rev Mex Fís. 2018;64(4 Jul–Aug):420–8. doi:10.31349/RevMexFis.64.420.
17. Bano A, Sajid M, Mahmood K, Rana MA. An oblique stagnation point flow towards a stretching cylinder with heat transfer. Phys Scr. 2020;95(1):015704. doi:10.1088/1402-4896/ab4772.
18. Booker JR. Thermal convection with strongly temperature-dependent viscosity. J Fluid Mech. 1976;76(4):741–54. doi:10.1017/S0022112076000876.
19. Wall DP, Wilson SK. The linear stability of channel flow of fluid with temperature-dependent viscosity. J Fluid Mech. 1996;323:107–32. doi:10.1017/S0022112096000869.
20. Nguyen CT, Desgranges F, Roy G, Galanis N, Maré T, Boucher S, et al. Temperature and particle-size dependent viscosity data for water-based nanofluids-Hysteresis phenomenon. Int J Heat Fluid Flow. 2007;28(6):1492–506. doi:10.1016/j.ijheatfluidflow.2007.02.004.
21. Prasad KV, Pal D, Umesh V, Prasanna Rao NS. The effect of variable viscosity on MHD viscoelastic fluid flow and heat transfer over a stretching sheet. Commun Nonlinear Sci Numer Simul. 2010;15(2):331–44. doi:10.1016/j.cnsns.2009.04.003.
22. Anjali Devi SP, Prakash M. Temperature dependent viscosity and thermal conductivity effects on hydromagnetic flow over a slendering stretching sheet. J Niger Math Soc. 2015;34(3):318–30. doi:10.1016/j.jnnms.2015.07.002.
23. Huda AB, Akbar NS. Heat transfer analysis with temperature-dependent viscosity for the peristaltic flow of nano fluid with shape factor over heated tube. Int J Hydrog Energy. 2017;42(39):25088–101. doi:10.1016/j.ijhydene.2017.08.054.
24. Alabdan R, Khan SU, Al-Qawasmi AR, Vakkar A, Tlili I. Applications of temperature dependent viscosity for Cattaneo-Christov bioconvection flow of couple stress nanofluid over oscillatory stretching surface: a generalized thermal model. Case Stud Therm Eng. 2021;28:101412. doi:10.1016/j.csite.2021.101412.
25. Ahmad U, Ashraf M, Al-Zubaidi A, Ali A, Saleem S. Effects of temperature dependent viscosity and thermal conductivity on natural convection flow along a curved surface in the presence of exothermic catalytic chemical reaction. PLoS One. 2021;16(7):e0252485. doi:10.1371/journal.pone.0252485.
26. Sheikholeslami M, Shamlooei M. Magnetic source influence on nanofluid flow in porous medium considering shape factor effect. Phys Lett A. 2017;381(36):3071–8. doi:10.1016/j.physleta.2017.07.028.
27. Waqas H, Farooq U, Muhammad T, Manzoor U. Importance of shape factor in Sisko nanofluid flow considering gold nanoparticles. Alex Eng J. 2022;61(5):3665–72. doi:10.1016/j.aej.2021.09.010.
28. Hayat U, Shaiq S, Shahzad A, Khan R, Kamran M, Ali Shah N. The effect of particle shape on flow and heat transfer of Ag-nanofluid along stretching surface. Chin J Phys. 2023;85:708–21. doi:10.1016/j.cjph.2023.02.008.
29. Khan AU, Nadeem S, Hussain ST. Phase flow study of MHD nanofluid with slip effects on oscillatory oblique stagnation point flow in view of inclined magnetic field. J Mol Liq. 2016;224:1210–9. doi:10.1016/j.molliq.2016.10.102.
30. Rizwana R, Hussain A, Nadeem S. Slip effects on unsteady oblique stagnation point flow of nanofluid in a view of inclined magnetic field. Math Probl Eng. 2020;2020:6580409. doi:10.1155/2020/6580409.
31. Kolsi L, Abbasi A, Alqsair UF, Farooq W, Omri M, Khan SU. Thermal enhancement of ethylene glycol base material with hybrid nanofluid for oblique stagnation point slip flow. Case Stud Therm Eng. 2021;28:101468. doi:10.1016/j.csite.2021.101468.

32. Mandal PK, Seth GS, Sarkar S, Chamkha A. A numerical simulation of mixed convective and arbitrarily oblique radiative stagnation point slip flow of a CNT-water MHD nanofluid. J Therm Anal Calorim. 2021;143(3):1901–16. doi:10.1007/s10973-020-10344-3.
33. Bai Y, Tang Q, Zhang Y. Unsteady MHD oblique stagnation slip flow of Oldroyd-B nanofluids by coupling Cattaneo-Christov double diffusion and Buongiorno model. Chin J Phys. 2022;79:451–70. doi:10.1016/j.cjph.2022.09.013.
34. Rahman MM, Grosan T, Pop I. Oblique stagnation-point flow of a nanofluid past a shrinking sheet. Int J Numer Meth Heat Fluid Flow. 2016;26(1):189–213. doi:10.1108/HFF-10-2014-0315.
35. Abbas N, Saleem S, Nadeem S, Alderremy AA, Khan AU. On stagnation point flow of a micro polar nanofluid past a circular cylinder with velocity and thermal slip. Results Phys. 2018;9:1224–32. doi:10.1016/j.rinp.2018.04.017.
36. Benkhedda M, Boufendi T, Tayebi T, Chamkha AJ. Convective heat transfer performance of hybrid nanofluid in a horizontal pipe considering nanoparticles shapes effect. J Therm Anal Calorim. 2020;140(1):411–25. doi:10.1007/s10973-019-08836-y.
37. Kata S, Ganganapalli S, Kuppalapalle V. Transport of thermal energy in the magnetohydrodynamic oblique stagnation point flow in a hybrid nanofluid with nanoparticle shape effect. Heat Trans. 2022;51(5):4331–48. doi:10.1002/htj.22502.
38. Li S, You X. Shape-factor impact on a mass-based hybrid nanofluid model for homann stagnation-point flow in porous media. Nanomater. 2023;13(6):984. doi:10.3390/nano13060984.
39. Rafique K, Mahmood Z, Alqahtani H, Eldin SM. Various nanoparticle shapes and quadratic velocity impacts on entropy generation and MHD flow over a stretching sheet with joule heating. Alex Eng J. 2023;71:147–59. doi:10.1016/j.aej.2023.03.021.
40. Rosalind Mary GL, Sreelakshmi K, Adnan, Khan SU, Mir A, Alshammari BM, et al. Applications of nonlinear thermal radiation on performance of hybrid nanofluid (Al_2O_3-Ag)/($C_2H_6O_2$-H_2O) for stagnation point flow: Blade and spherical shaped nanoparticles. J Radiat Res Appl Sci. 2024;17(4):101171. doi:10.1016/j.jrras.2024.101171.
41. Asghar Z, Khan MWS, Gondal MA. Numerical analysis of Carreau fluid inside a horizontal passage with axial conduction and viscous dissipation: an extended Graetz problem. J Therm Anal Calorim. 2024;149(14):7527–35. doi:10.1007/s10973-024-13332-z.
42. Baazeem AS, Arif MS, Abodayeh K. An efficient and accurate approach to electrical boundary layer nanofluid flow simulation: A use of artificial intelligence. Processes. 2023;11(9):2736. doi:10.3390/pr11092736.
43. Nawaz Y, Shoaib Arif M, Abodayeh K, Hassan Soori A. A two-stage multi-step numerical scheme for mixed convective Williamson nanofluid flow over flat and oscillatory sheets. Int J Mod Phys B. 2024;38(22):2450298. doi:10.1142/s0217979224502989.
44. Muhammad K, Alrihieli HF, Allehiany FM, Gamaoun F. Comparative study of stagnation point nanofluid flow with partial slips using shooting technique. J Therm Anal Calorim. 2024;149(4):1715–24. doi:10.1007/s10973-023-12736-7.